Brain Topography (2019) 32:583–598
https://doi.org/10.1007/s10548-018-0623-1

ORIGINAL PAPER

Mapping Brain Activity with Electrocorticography: Resolution Properties and Robustness of Inverse Solutions

Chiara Todaro[1] · Laura Marzetti[1,2] · Pedro A. Valdés Sosa[3,4] · Pedro A. Valdés-Hernandez[5] · Vittorio Pizzella[1,2]

Received: 12 January 2017 / Accepted: 16 January 2018 / Published online: 23 January 2018

Abstract

Electrocorticography (ECoG) is an electrophysiological technique that records brain activity directly from the cortical surface with high temporal (ms) and spatial (mm) resolution. Its major limitations are in the high invasiveness and in the restricted field-of-view of the electrode grid, which partially covers the cortex. To infer brain activity at locations different from just below the electrodes, it is necessary to solve the electromagnetic inverse problem. Limitations in the performance of source reconstruction algorithms from ECoG have been, to date, only partially addressed in the literature, and a systematic evaluation is still lacking. The main goal of this study is to provide a quantitative evaluation of resolution properties of widely used inverse methods (eLORETA and MNE) for various ECoG grid sizes, in terms of localization error, spatial dispersion, and overall amplitude. Additionally, this study aims at evaluating how the use of simultaneous electroencephalography (EEG) affects the above properties. For these purposes, we take advantage of a unique dataset in which a monkey underwent a simultaneous recording with a 128 channel ECoG grid and an 18 channel EEG grid. Our results show that, in general conditions, the reconstruction of cortical activity located more than 1 cm away from the ECoG grid is not accurate, since the localization error increases linearly with the distance from the electrodes. This problem can be partially overcome by recording simultaneously ECoG and EEG. However, this analysis enlightens the necessity to design inverse algorithms specifically targeted at taking into account the limited field-of-view of the ECoG grid.

Keywords Electrocorticography · Electroencephalography · Resolution metrics · eLORETA · MNE

Introduction

Electrocorticography (ECoG) is a neuroimaging technique which records, directly on the cortical surface, the electric potential generated by neural currents. In order to reach the surface of the cortex, a craniotomy is necessary, thus ECoG is performed on human subjects only in clinical applications, e.g., in pharmacoresistant epilepsy for which surgery is already planned. The ECoG signals are recorded by stainless steel electrodes embedded in silastic strips, usually housing tens of electrodes. In order to limit the chance of infection, the strips don't cover the entire cortical surface but are inserted right above the areas that have to be mapped in view of a possible surgical intervention. The strips are designed with enough flexibility to ensure that cortical regions not exposed by the craniotomy can still be, at least partially, reached, thus allowing for a broader, although still spatially limited, brain mapping.

High invasiveness and limited coverage are the main drawbacks of ECoG. However, ECoG benefits from high temporal (ms) and spatial (mm) resolution and features a signal-to-noise ratio (SNR) much higher than that of non-invasive techniques such as Electroencephalography (EEG), in which the low conductivity of the skull attenuates scalp potentials. For these unique advantages, ECoG signals have been successfully used for clinical purposes: e.g., identify epileptogenic zones (Ortega et al. 2008) and predict the success of surgical resection (Sugano et al. 2007). Indeed, the

Handling Editor: Christoph M. Michel.

This is one of several papers published together in Brain Topography on the "Special Issue: Controversies in EEG Source Analysis".

Electronic supplementary material The online version of this article (https://doi.org/10.1007/s10548-018-0623-1) contains supplementary material, which is available to authorized users.

✉ Chiara Todaro
chiara.todaro@unich.it

Extended author information available on the last page of the article

high SNR of the ECoG signals allowed to use them as gold standard to characterize epileptogenic zones identified by the source estimates obtained from non-invasive techniques, e.g. EEG and Magnetoencephalography (MEG) (Ding et al. 2007; de Gooijer-van de Groep et al. 2013).

At the same time, data recorded for diagnosis have allowed to address a limited number of neuroscience questions: e.g., map cortical functions (Potes et al. 2012; Gunduz et al. 2012; Mesgarani and Chang 2012), and investigate functional mechanisms of brain oscillations (Crone et al. 1998; Daitch et al. 2013; Watrous et al. 2015). A more extensive use of ECoG is possible in nonhuman primates, where a mapping of the activity of a larger portion of the cortex is feasible (Yanagawa et al. 2013; Takaura et al. 2016). Nevertheless, the partial coverage of the ECoG grid still limits application in cognitive studies. For example, in research experiments where a human patient undergoes ECoG, often the cortical areas involved in the cognitive process of interest are not directly located below the electrodes, since the grid placement is led by clinical requirements with no reference to neuroscientific purposes. The same problem may arise in clinical studies, when the ECoG grid is misplaced because of a wrong presurgical evaluation. Thus, to study these areas it is necessary to reconstruct brain activity from the measured ECoG potentials by solving the corresponding electromagnetic inverse problem, and this also has the additional advantage of overcoming the reference electrode issue. Indeed, ECoG potentials depend on the chosen reference electrode or on the offline re-referencing scheme (Liu et al. 2015), in analogy to the EEG case (Neuper and Klimesch 2006; Marzetti et al. 2007; Chella et al. 2016).

The technical aspects involved in solving the ECoG inverse problem have a great overlap with those pertaining to the EEG inverse problem. Certainly, source reconstruction literature for EEG has a long-lasting tradition and many different inverse algorithms have been explored [for a review see Michel et al. (2004) and Grech et al. (2008)], with the EEG expertise having thus been a natural starting point for ECoG researchers.

The advantages and disadvantages of source reconstruction from EEG data have been largely discussed in literature (Koles 1998; Michel et al. 2004). Given the clear advantages of being able to reconstruct the source activity inside the brain with improved spatial resolution, the disadvantage of this procedure is in the ill-posedness of the inverse problem, i.e. the non-uniqueness of the solution and its instability with respect to noise. On the one side, being the ECoG grid directly placed above the cortical surface, the high SNR of the recorded signals allows to obtain robust solutions, at least under the electrodes. On the other side, since the coverage of the ECoG grid is limited, data contain poor information from sources not directly covered by the electrodes. Despite these issues, in the last years, steps forward have been made toward an accurate source reconstruction of neural sources located under the ECoG grid (Zhang et al. 2008; Dümpelmann et al. 2009, 2012; Pascarella et al. 2016), with a significant improvement in the ability to identify also deep and nearby sources (Cho et al. 2011) in respect to the ECoG potentials.

To date, an extensive characterization of the performance of various inverse methods at different brain sites, especially for sources laying far from the ECoG electrodes, for different electrode arrangements, and for simultaneous ECoG and EEG still lacks in the literature. The study from Zhang et al. (2008) has shown that the higher SNR of ECoG turns into an improvement in the localization accuracy of the reconstructed activities for sources located underneath the ECoG grid while, far from the ECoG electrodes, EEG outperforms ECoG in localization accuracy. This study is the first that has quantitatively investigated the performance of inverse methods in ECoG, although it simulates a restricted number of source configurations, and uses the sole localization error to characterize the inverse solver properties. Indeed, making inferences about the performance of inverse solvers on the basis of the localization error alone has been shown to be not sufficient for configurations consisting in more than one source (Molins et al. 2008; Hauk et al. 2011).

In this paper, we extend the results obtained by Zhang et al. by simulating data from a combined grid layout consisting in a 128 channels ECoG and a 18 channels EEG in a realistic monkey set-up[1] which was also used in Papadopoulou et al. (2015). In our case, this set-up is ideal to address the controversial issue of the usefulness of source localization far from the electrodes for ECoG data. In this study, this issue will be addressed by posing two specific questions:

(i) How far from the brain regions directly covered by the ECoG electrode grid it is possible to obtain reliable source estimation?
(ii) Can ECoG source reconstruction performance be improved by integration with simultaneous EEG?

These questions will be here addressed by a quantitative analysis of the performance of two inverse methods: eLORETA (Pascual-Marqui 2007) and MNE (Hämäläinen et al. 1993). This analysis uses the resolution metrics described by Hauk et al. (2011) and takes into account several performance indicators: the dipole localization error (mislocalization), the spatial dispersion (spread of the activity for point-like sources),

[1] This data-set was proposed in the "Controversies in EEG source analysis" workshop (Chengdu, China, 2014) and consists in simultaneous ECoG and EEG recordings performed on a specimen of *Macaca mulatta* and in the corresponding lead field matrices calculated by Pedro A. Valdes-Hernandez.

and the overall amplitude (relative sensibility across cortical locations).

Materials and Methods

The ECoG Inverse Problem

The ECoG inverse problem, i.e. the estimate of the current sources **J** inside the brain that generate the observed electric potentials **V**, can be expressed through:

$$V = L \cdot J \tag{1}$$

where the symbol · indicates matrix product and **L** is the so called lead field matrix or forward operator. The lead field matrix is a linear operator incorporating the conduction properties of the head model (that must be known in advance) and describing the contribution of each brain source to each channel. In our case, the sources can be represented as a discrete set of unitary current dipoles in the whole cortex, referred to as source space, which model small patches of cortical sheet with an area of a few mm^2. Each current dipole is characterized by its position, magnitude and orientation. The dipole orientation is often supposed to be normal to the cortical surface, whose small patches can be punctually approximated as a plane surface. This assumption will hold throughout the following text.

To the aim of solving the inverse problem, an estimate of the current $\hat{\mathbf{J}}$ must be calculated by means of a given inverse operator **T**, such that

$$\hat{J} = T \cdot V \tag{2}$$

Unfortunately, the electromagnetic inverse problem is inherently ill-posed since a set of ECoG observations can be associated to multiple (infinite) solutions; nevertheless, the use of *a priori* information on source parameters allows to find a unique solution for $\hat{\mathbf{J}}$. Different choices of *a priori* information result into different inverse operators **T** with different properties. In this paper, we will use two specific algorithms for the solution of the inverse problem: the exact Low Resolution Electromagnetic Tomography (eLORETA) and the Minimum Norm Estimate (MNE). These approaches have been chosen since they are widely used for electromagnetic source reconstruction; in particular, we used the implementations given in the FieldTrip toolbox (Oostenveld et al. 2011). In the following, these inverse operators are briefly described.

The eLORETA solver, extensively described in Pascual-Marqui (2007), is characterized by zero localization error for point-like test sources in the presence of measurement and structured biological noise. The inverse operator matrix for eLORETA is defined as

$$T_{eLORETA} = W^{-1} \cdot L^t \cdot \left(L \cdot W^{-1} \cdot L^t + \alpha I\right)^{\dagger} \tag{3}$$

where α is the regularization parameter, **I** is the identity matrix, † is the Moore–Penrose pseudoinverse operator and **W** is a diagonal weighting matrix. Each diagonal element $\mathbf{W_i}$ corresponds to the i-th element of the source space (e.g. the discretized cerebral cortex) and can be written as

$$W_i = \left[L_i^t \cdot \left(L \cdot W^{-1} \cdot L^t + \alpha I\right)^{\dagger} \cdot L_i\right]^{\frac{-1}{2}} \tag{4}$$

where $\mathbf{L_i}$ is the i-th column of the lead field matrix **L**. The matrix **W** is chosen such that the estimated current covariance matrix has the minimum difference, in the least square sense, with the identity matrix. It has been shown that this procedure reaches zero localization error for each point-like source in the whole cortical surface (Pascual-Marqui 2007).

The MNE algorithm (Hämäläinen et al. 1993) requires that the estimated neural current fits the measured data in the least square sense while having the minimum power. The resulting inverse operator is

$$T_{MNE} = L^t \cdot \left(L \cdot L^t + \alpha C\right)^{-1} \tag{5}$$

where α is the regularization parameter and C is the covariance matrix of the noise.

The MNE method is known to suffer from overestimation of superficial sources which can be partially solved by means of depth weighting correction (Lin et al. 2006) and noise normalization (Dale et al. 2000). In this study, we apply depth weighting correction by normalizing each column of the lead field matrix by its l_2 norm, while we assume that the noise is Gaussian, white, independent and identically distributed between channels, thus $\mathbf{C} = \mathbf{I}$ in Eq. (5).

In particular, the regularization parameter is chosen to be inversely proportional to the SNR and to the number of electrodes in the grid and directly proportional to the trace of the first term that must be regularized in Eqs. (3) and (5), for eLORETA and MNE, respectively. In the case of noiseless data, the regularization parameter is estimated using a value of SNR = 1000.

Resolution Metrics

To assess the ability of a given inverse method to accurately estimate the neural currents, it is possible to evaluate the relationship between the estimated current $\hat{\mathbf{J}}$ and the actual (unknown) current **J** by means of the resolution matrix, namely **R**.

From combining Eqs. (1) and (2), $\hat{\mathbf{J}}$ can be related to **J** as in the following

$$\hat{J} = T \cdot V = T \cdot (L \cdot J) = R \cdot J \qquad where\ R = T \cdot L \tag{6}$$

The resolution matrix **R** has as many rows as columns, equal to the number of unknowns, i.e. the number of sources. By definition, **R** depends on the lead field matrix **L**, which,

in turn, depends on the electrode grid geometry, on the source space and on the head model. In case of perfect source reconstruction (i.e., $\hat{\mathbf{J}} = \mathbf{J}$), the resolution matrix would be the identity matrix, as is clearly seen from the third equality in Eq. (6). Practically, non-zero off-diagonal elements in $\mathbf{R}$ arise due to distortions in the reconstructed cortical activity. To characterize the influence of the off-diagonal elements on source reconstruction, the columns and rows of $\mathbf{R}$ must be considered. From here on, following the definition given by Hauk et al. (2011) and Hauk and Stenroos (2014), we will refer to each column of $\mathbf{R}$ as the point spread function (PSF) and to each row of $\mathbf{R}$ as the cross-talk function (CTF). Specifically, each column of $\mathbf{R}$ expresses how the activity of a single source in a specific brain location spreads out, in the reconstruction process, over the whole cortical surface; while each row of $\mathbf{R}$ expresses how the activity of all sources throughout the brain affects the reconstruction of the activity in a specific brain location. Moreover, to quantify the distortion in source reconstruction related to either the PSF or the CTF, we rely on the metrics described by Molins et al. (2008) and Hauk et al. (2011), namely: the dipole localization error (DLE), the spatial dispersion (SD), and the overall amplitude (OA). The definition of these metrics is recalled in the following paragraph for the reader's convenience.

For a given dipolar source located at $\mathbf{x_i}$, let $\mathbf{r_i}$ be, with abuse of notation, either a column or a row of $\mathbf{R}$, i.e., the corresponding PSF or CTF, and $(\mathbf{r_i})_\mathbf{j}$ the j-th element of vector $\mathbf{r_i}$. Thus, the DLE, SD, and OA metrics are defined as

$$DLE_i = \left\| \boldsymbol{x}_p - \boldsymbol{x}_i \right\|_2 \quad where \quad p = argmax\left(\boldsymbol{r}_i\right) \tag{7}$$

$$SD_i = \sqrt{\frac{\sum_j \left[d_{ij}\left(\boldsymbol{r}_i\right)_j \right]^2}{\sum_j \left[\left(\boldsymbol{r}_i\right)_j \right]^2}} \qquad where \;\; d_{ij} = \left\| \boldsymbol{x}_i - \boldsymbol{x}_j \right\|_2 \tag{8}$$

$$OA_i = \sum_j \left| \left(\boldsymbol{r}_i\right)_j \right| \qquad (normalized\ to\ max_i OA_i) \tag{9}$$

The DLE represents the Euclidean distance between the position of i-th source and that of the estimated one[2], in our notation $\mathbf{x_i}$ and $\mathbf{x_p}$, respectively. The ideal DLE value is zero, indicating exact spatial localization.

The SD expresses the spreading radius of the reconstructed activity of the i-th source, weighted by the distance of the source from all the other sources. The ideal SD value is zero, indicating no spatial spread for a point-like source.

The OA is the normalized sensitivity profile, i.e., sources with a higher OA value correspond to "powerful" locations the activity of which is overestimated with respect to "weaker" locations. The OA values lay in the range [0, 1] by definition, and, in the ideal case, are uniform over the cortex indicating no over- or underestimated locations.

The above metrics altogether allow to evaluate the resolution properties of the source reconstruction algorithms in the absence of noise. Here, we rely on DLE, SD, and OA for the PSF and the CTF of eLORETA and MNE inverse algorithms to assess their performance while varying grid layouts. Specifically, we varied: the number of channels in the ECoG grid, the grid position over the cortical surface, and the combination of the ECoG grid together with the EEG grids.

Source Space and Grid Layout

The source space and ECoG and EEG grid layouts used in this study is derived from the publicly available data presented in the workshop entitled "Controversies in EEG Source Imaging" held on August 2014 in Chengdu, China. In particular, we used the set-up corresponding to the "monkey Su" data released by Naotaka Fujii (http://www.neurotycho.org) consisting in simultaneous ECoG and EEG recordings from a female specimen of *Macaca mulatta* [for more details see Nagasaka et al. (2011)]. The electrode grids are briefly described below:

- ECoG grid with 128 electrodes embedded in a 1 mm-thick silicone sheet, covering almost entirely the left hemisphere with a mean electrode spacing of around 5 mm.
- EEG grid with 18 electrodes positioned according to the standard 10–20 electrode system in which the Cz channel was removed to avoid contact with one ECoG connector. Of note this grid covers the whole brain, with a mean distance of about 30 mm between nearby electrodes (but for Cz).

To model the monkey's head for solving the electromagnetic forward problem, four compartments were taken into account: the brain (enclosed by the pial surface) together with the surrounding cerebrospinal fluid, the skull, the skin and the silicone sheet holding the ECoG electrodes. In each compartment, the electrical conductivity is assumed to be constant. Specifically, the conductivity ratio between consecutive compartments was set to 1/25 for skull-to-other brain layers, while, being the silicone layer conductivity very low, its conductivity was set to a negligible value compared to other compartments.

[2] For imaging methods for solving the inverse problem, a source is often referred to as a local maximum in the reconstructed activity.

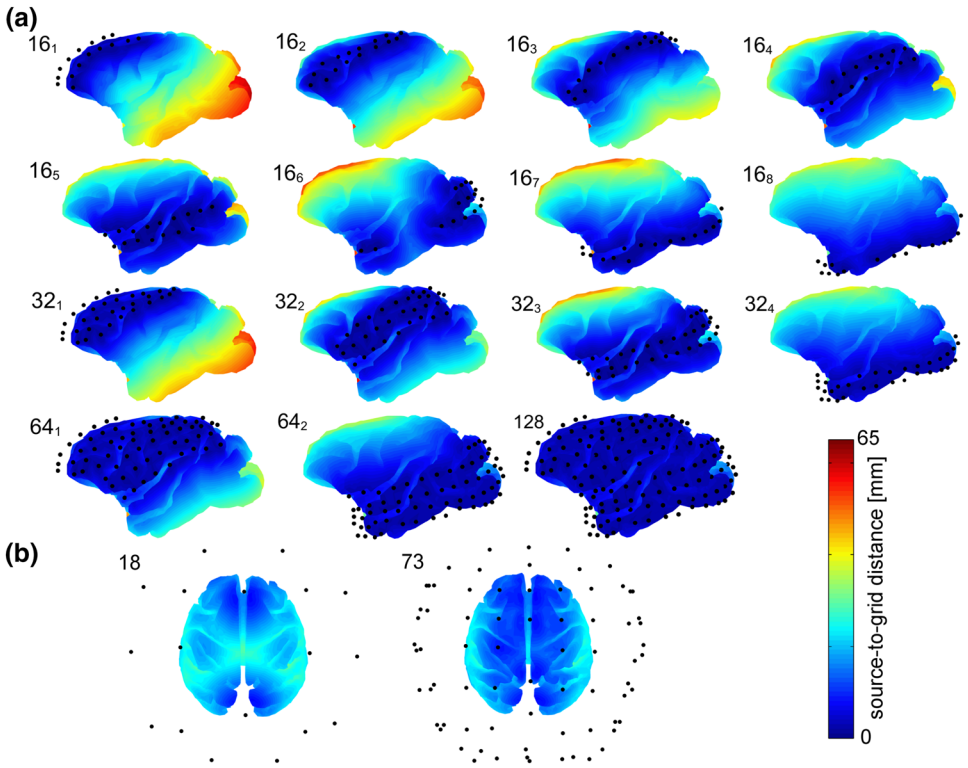

Fig. 1 ECoG (**a**) and EEG (**b**) grid layouts. For each grid, every point of the cortex is color coded according to its source-to-grid distance

A high resolution source space, spanning the whole cortical surface and modeled by a mesh consisting of 104,650 vertices (source positions) and 209,300 triangles was provided in the original data set. This source space considered a free orientation for each source. For computational reasons, in this work the Edge-Collapse method implemented in the open-source 3D computer graphics software Blender (http://www.blender.org/) was used to down-sample the high resolution source space to 5232 vertices and 10,464 triangles with a distance constraint of 3 mm between every vertex and at least one of its neighbors. Additionally, since we have assumed the orientation of the sources to be normal to the cortical surface, we fixed the source orientation as the sum of the normal vectors of the mesh triangles adjacent to the selected vertex.

The ECoG and the EEG lead field matrices were originally calculated by using the Finite Element Method implemented in the software NeuroFEM (http://www.mrt.uni-jena.de/simbio). Consistently with the cortical mesh, the lead field matrices were downsampled to 5232 sources with direction normal to the cortical surface.

Starting from the ECoG grid with 128 electrodes, we defined smaller sub-grids by splitting the original layout in such a way that all the sub-grids together cover the same portion of the cortex covered by the full grid. This procedure led to the definition of two 64 electrode grids, four 32 electrode grids and eight 16 electrode grids.

Furthermore, we simulated a dense EEG grid with 73 channels, accordingly to the 10–10 system (inter-electrodes distance of around 15 mm), starting from the 18 channels EEG grid. We choose this set-up to quantify to what extent increasing the number of EEG electrodes increases the resolution of the ECoG + EEG grid layout in a more realistic human scenario where most often high-density EEG grid is used. Figure 1 shows the defined sub-grids and, for each sub-grid, the Euclidean distance between every vertex in the cortical mesh and the nearest electrode of the sub-grid, i.e., the source-to-grid distance. We divided the source space into distance classes spanning 5 mm each: sources in the first class have a source-to-grid distance strictly less than 5 mm; sources in the second class feature a source-to-grid distance between 5 and 10 mm; etc.

The resolution matrices for eLORETA and MNE for each of the constructed ECoG grids were calculated, together with the DLE, SD and OA metrics for the PSF and the CTF. To asses these metrics for a given source-to-grid distance class, we averaged together the corresponding values for all points within that class.

The same strategy was used for the combination of each of the ECoG sub-grids (including the original 128 electrodes grid) with the EEG array of 18 channels.

Influence of Gaussian Noise

The analysis of the PSF of the resolution matrix provides information about the noise-free cases in which one source is active at a time. However, in real applications the electrical potential recorded by the electrode grid is contaminated by noise. In order to investigate the influence of different levels of noise on the resolution metrics we estimated the neural activity from data generated by one simulated dipole with superimposed Gaussian noise to account for different levels of SNR (20, 10 and 3 dB).

For each dipole in the source space, we simulated the noisy data generated by such dipole, we reconstructed the PSF with eLORETA and MNE, and then we calculated DLE, SD, and OA values. We repeated this procedure for each level of SNR and for different grids. We chose two representative grids to reconstruct the source activities: the 128 channels ECoG grid, and the ECoG + EEG grid with 128 + 18 channels. As well as for the noise-free case, we studied the resolution metrics as a function of the source-to-grid distance by averaging together all the points belonging to the same distance class for every level of SNR.

Extending the concept of the PSF previously defined, we can interpret the estimated activity as a "noisy PSF". This idea cannot be extended to identify the analogous of the "noisy CTF" using the resolution matrix, which we defined under the noise-free assumption [see Eq. (6)]. Nevertheless, further considerations on the influence of noise on the resolution matrix will be addressed in the "Discussion" section.

Results

Figure 2 summarizes the results for the chosen resolution metrics as defined in Eqs. (7), (8) and (9). For each of the ECoG grid layouts as defined above, the DLE, SD and OA are given as a function of the source-to-grid distance classes. Specifically, the first and second rows show the results for DLE, SD and OA for the eLORETA- and MNE-PSF, respectively. Similarly, the third and the fourth rows show the corresponding results for the CTF. It can be observed that DLE values (Fig. 2, first column) increase for increasing source-to-grid distance for both PSFs and CTFs for all the ECoG grids and both inverse algorithms, the only exception being the eLORETA-PSF-DLE which is always zero by construction (Pascual-Marqui 2007). The other DLE values, i.e. for MNE-PSF, MNE-CTF and eLORETA-CTF, are mainly influenced by the source-to-grid distance, irrespectively of the grid position and the number of electrodes. The difference in DLEs between the various grids observed for source-to-grid distances in the higher distance classes is not significant, rather it is due to the lower number of sources pertaining to those classes. Indeed, the average DLE values in each class have a larger uncertainty when estimated from a low number of sources.

On the other hand, the SD values (Fig. 2, second column), which also increase for increasing source-to-grid distance for both PSF and CTF for all the ECoG grids and both inverse algorithms, are also influenced by the number of electrodes in the grid. Indeed, grids with 16 electrodes show, for all source-to-grid distances, the highest SD values, while grids with 32 and 64 electrodes have intermediate values and the 128 electrode grid features the smallest values. This effect is more evident for the eLORETA-PSF-SD (Fig. 2, second column, first row). In fact, a direct comparison of the SD results for eLORETA and MNE shows clear differences for both the PSF- and the CTF-SD. Specifically, the eLORETA-PSF-SD values lie in the range 10–35 mm, being loosely related to the source-to-grid distance for each grid, while the MNE-PSF-SD values show a clear positive relation with the source-to-grid distance for each grid, with lower values for classes characterized by small source-to-grid distances. The high spatial accuracy of eLORETA-PSF-DLE comes at the expenses of the larger PSF-SD values, but not for the CTF values, in accordance with Hauk et al. (2011).

Additionally, the eLORETA-CTF-SD values show, for each grid, a steeper dependence on the source-to-grid distance in comparison to the corresponding MNE values, resulting in a wider spatial spread for eLORETA at distances larger than 20 mm. For these distances, indeed, the eLORETA-CTF-SD values lie in the range 20–55 mm while the corresponding MNE values lie in the range 20–35 mm. At distances lower than 20 mm, the MNE-CTF-SD values show worse performances in comparison to eLORETA-CTF-SD. It should be noted that, for MNE, all the metrics calculated for PSF and CTF have identical profiles as expected from the fact that the MNE resolution matrix is symmetric (Hauk et al. 2011; Hauk and Stenroos 2014).

Finally, the OA values (Fig. 2, third column) are strongly influenced by the number of electrodes, the inverse algorithm and the PSF or CTF case. The OA values are normalized to the maximum of the average OA values in each distance class. In the ideal resolution matrix, OA values are constantly equal to 1 in the whole cortex, being the ideal sensitivity profile equal for all sources. However, neither eLORETA nor MNE reaches this ideal condition. In the PSF case for both eLORETA and MNE the sources with higher OA values are those underneath the electrodes, being the dependence steeper for eLORETA than for MNE. Furthermore, OA range spans from 1 to 0 for eLORETA, and from 1 to 0.4 for MNE, hence eLORETA underestimates the most distant sources more than MNE. For eLORETA-CTF, there is an inverse trend, i.e. the sources with higher OA values do not lay underneath the grid, though in the whole brain OA values are always larger than 0.6.

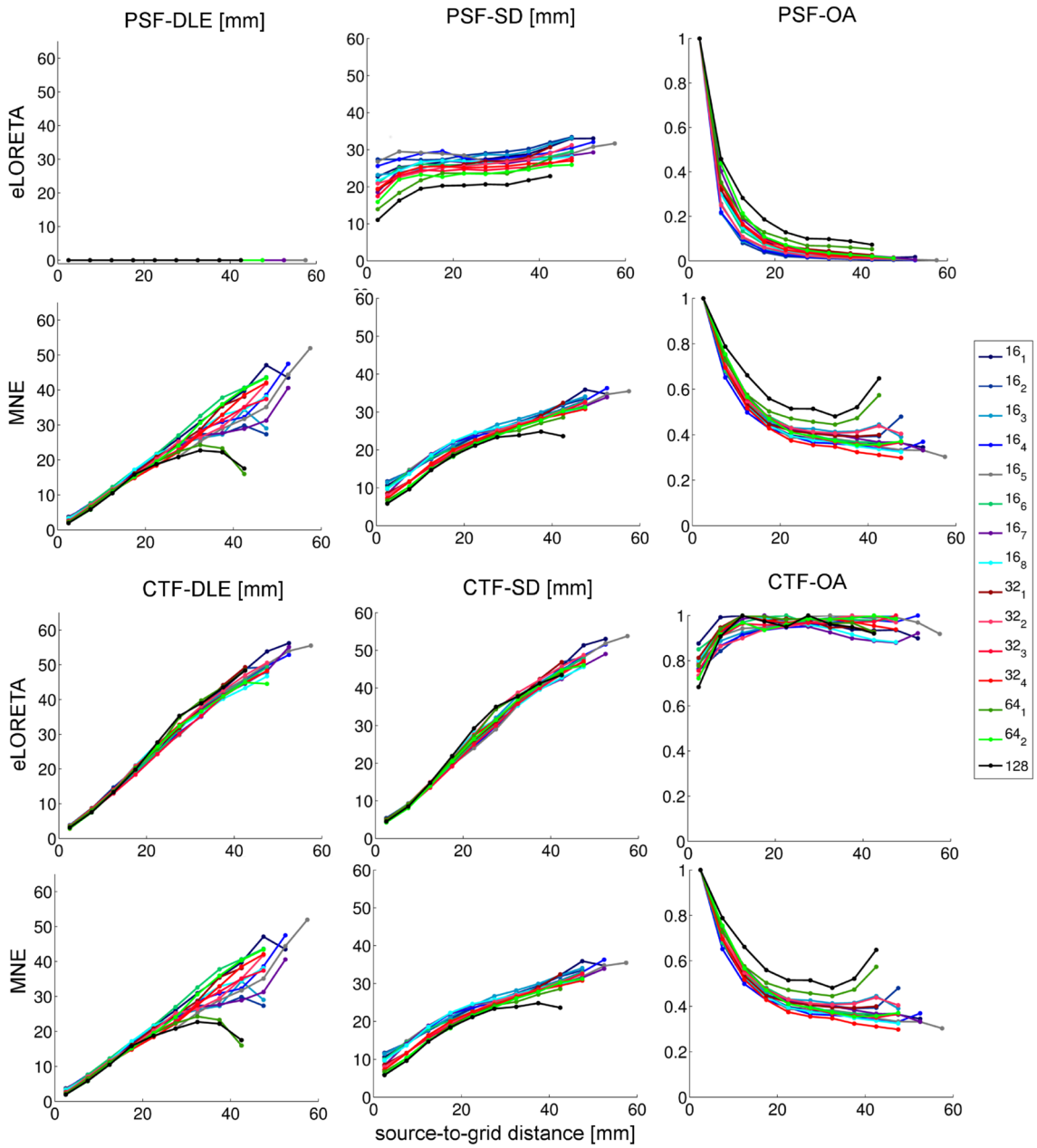

Fig. 2 Mean values of DLE, SD and OA of each distance class, calculated for every ECoG grid. Blue, red and green lines represent grids with 16, 32 and 64 electrodes, respectively. The black line refers to the ECoG grid with 128 electrodes

Overall, Fig. 2 shows that the resolution metrics calculated for MNE have a medium performance with respect to eLORETA. Indeed, in the PSF case the ideal value of eLORETA-DLE is balanced by the worst performance of eLORETA-SD values which are at least 5 mm higher than MNE-SD. In the CTF case eLORETA-DLE and -SD values grow steeper with the source-to-grid distance in respect to MNE-DLE and -SD, though MNE-SD are a few mm higher under the grid.

In order to investigate the effects of the combined ECoG and EEG recordings on the source reconstruction resolution, the above analysis has been replicated for the combination of all the ECoG grids with the 18 channels EEG grid.

Figure S1 from the Supplementary materials displays the same quantities shown in Fig. 2 for the combination of each ECoG grid with the EEG grid. The results for the EEG grid alone are represented as a yellow line. Note that the resolution metrics are averaged using the source-to-grid distance

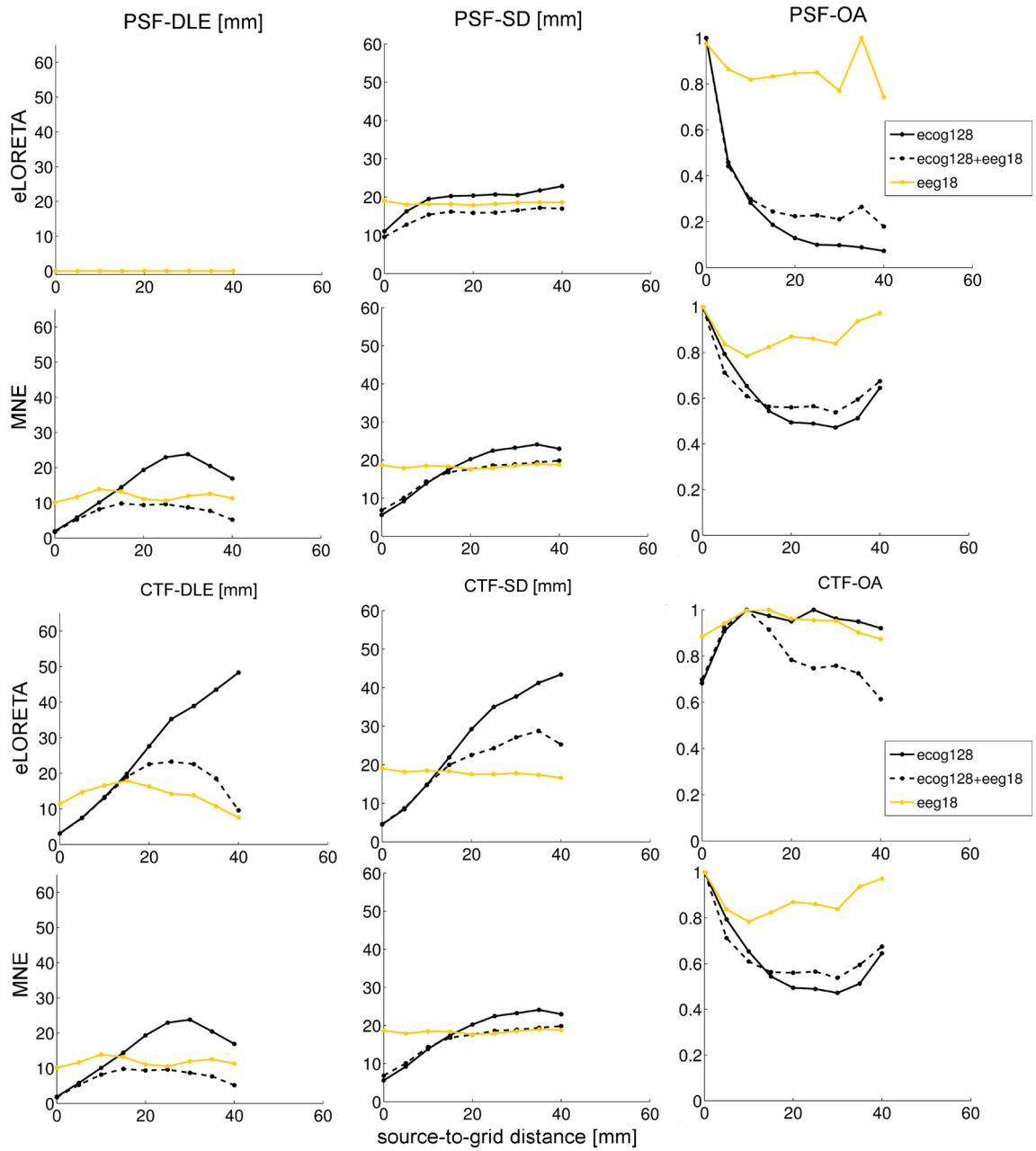

Fig. 3 Direct comparison between the ECoG and the ECoG + EEG grids as a function of the source-to-grid distance in a specific case. The mean values of PSF- and CTF-DLE, SD and OA of each distance class, are calculated for the 128 channels ECoG grid (black solid line), 128 + 18 channels ECoG + EEG grid (black dotted line) and 18 channels EEG grid (yellow line) with eLORETA and MNE

classes defined on the ECoG grids for a comparison with the results of Fig. 2. For the EEG alone case, the source-to-grid distance classes are calculated with respect to the 128 electrodes ECoG grid

A direct comparison between ECoG and ECoG + EEG is shown in Fig. 3 for the 128 channels ECoG and 18 channels EEG grids, being this specific case representative of the general trend of the resolution metrics for the multimodal layout.

We note two distinct behaviors for sources near and far from the ECoG grid. When considering sources close to the ECoG electrodes, the resolution metrics of the ECoG + EEG grid are very similar to the ones calculated for the ECoG grids alone. Indeed, for sources with a source-to-grid distance lower than 20 mm, practically EEG does not alter the ECoG results, the only exception being eLORETA-PSF-SD case in which the SD values lower, probably due to the increasing number of electrodes (see also figure S1 in the

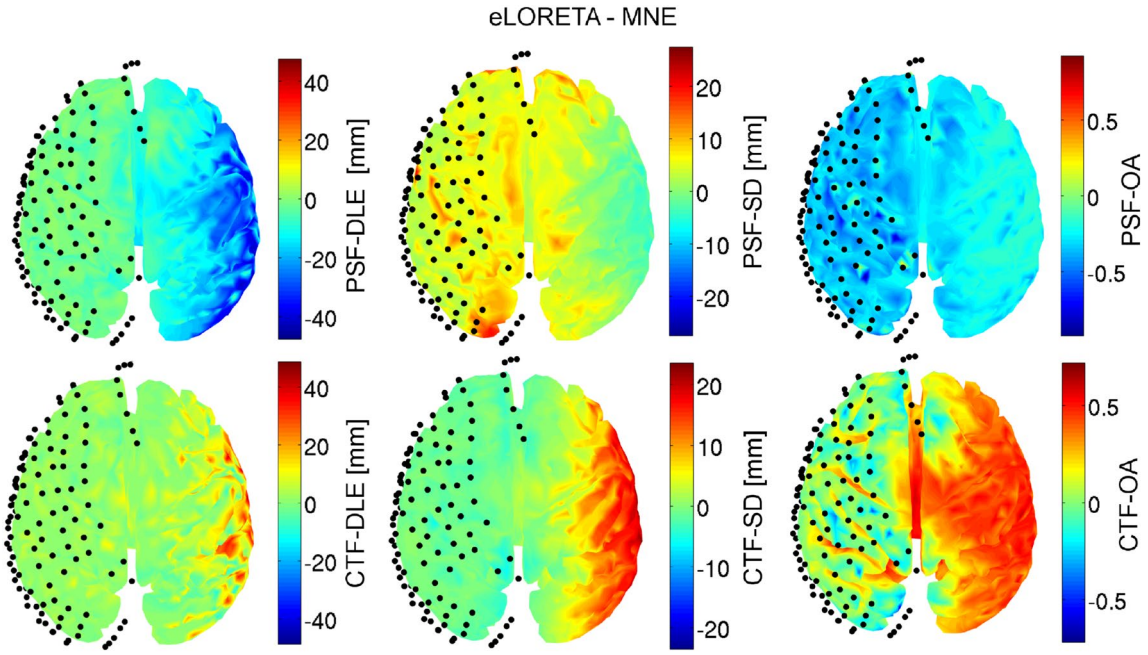

Fig. 4 Difference for every source on the cortex between eLORETA and MNE in the PSF and CTF cases for each metric with the 128 channels ECoG grid

supplementary material). When the distance of the sources from the ECoG grid is larger than 20 mm, the DLE and SD values no longer show a monotonic increase as previously observed in Fig. 2, but these values are close to those obtained for the EEG alone. Note that 20 mm represents a boundary for the source-to-grid distance: below 20 mm the sources are closer to the ECoG electrodes than to the EEG channels, thus it is clear that below this distance the results are dominated by ECoG other than by EEG.

For OA values there is a slight improvement, since the most distant sources have higher OA values when ECoG and EEG are recorded simultaneously than the same sources in the presence of ECoG alone. For example, eLORETA-PSF-OA values range from 1 to 0 for ECoG grids (Fig. 2, third column) while for the multimodal layout OA values range from 1 to 0.2 (Fig. S1, third column, supplementary material).

Even if this multimodal setting generally improves the resolution of the reconstructed sources, especially for distant sources, we note that the simultaneous recording of ECoG and EEG differently affects eLORETA and MNE inverse solutions. For MNE, the resolution properties of the ECoG + EEG grid are always better than those obtained using a single modality, while for eLORETA the combination of EEG with ECoG deteriorates the resolution metric values with respect to the EEG grid alone. Indeed, for the ECoG + EEG grid (black dotted line) eLORETA-CTF-DLE and -SD have higher values than the same metrics for the EEG grid (yellow solid line). This happens because the eLORETA inverse operator is iteratively calculated through the weight in Eq. (4) in which the product of the lead field matrix with its transpose is repeated for each iteration (see Pascual-Marqui (2007) for more details). Since the norm of the ECoG lead field matrix columns are larger than the EEG ones, the improvement in resolution brought by the EEG grid is not enough to significantly reduce the high CTF-DLE and -SD values of the ECoG grids.

Nevertheless, the improvement in accuracy in respect to ECoG grid alone is evident for all sources with a source-to-grid distance higher than 20 mm.

Metric Distributions Over the Cortex

The previous analyses (Figs. 2, 3 and S1) show the average trend of each metric with respect to source-to-grid distance classes regardless of the specific location over the cortex. It is also interesting to visualize the metric distributions on the whole cortical surface for different layouts, as shown in Figs. S2 and S3 for three representative grids: ECoG with 128 channels (first group of two rows), ECoG + EEG with 128 + 18 channels (second group of two rows) and ECoG + EEG with 16 + 18 channels together with EEG (third group of two rows) for both of the inverse algorithms. In particular, Figs. 4 and 5 enlighten differences over the whole cortical surface between the inverse algorithms and between the multimodal and single layout, respectively.

Figure 4 shows the differences between eLORETA and MNE for the 128 channels ECoG grid. In the Point-Spread

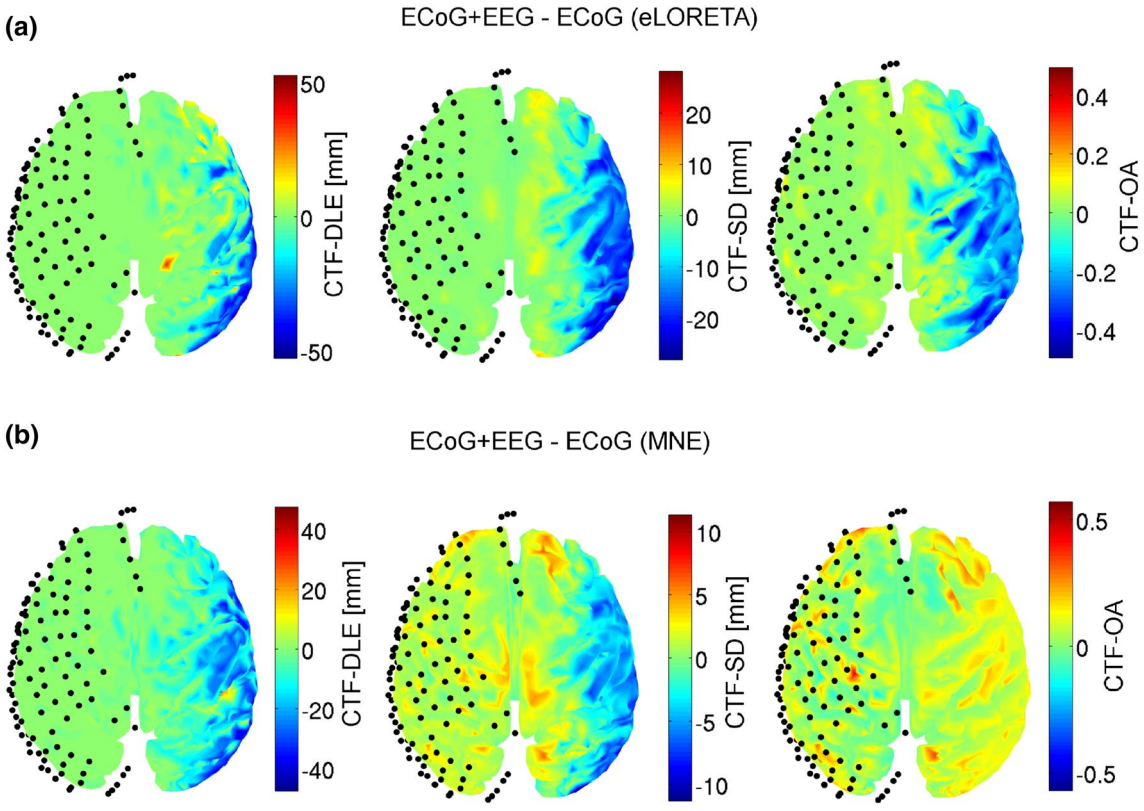

Fig. 5 Difference for every source on the cortex between the ECoG + EEG grid with 128 + 18 channels and the ECoG grid only with 128 channels in eLORETA-CTF (**a**) and in MNE-CTF (**b**) for each metric

Function (PSF) case, eLORETA has better results than MNE; indeed the dipole localization error (DLE) for eLORETA is lower, up to 40 mm, far from the electrodes, although the spatial dispersion (SD) for eLORETA is higher, up to 25 mm, under the electrodes. In the cross-talk function (CTF) case, MNE performs better than eLORETA, indeed the eLORETA-CTF-DLE and -SD have higher values far from the electrodes, up to 40 and 20 mm, respectively.

The overall amplitude (OA) distributions show larger differences between eLORETA and MNE. PSF-OA is lower for eLORETA than MNE, probably because MNE has a bias in overestimating sources towards the electrodes. This can be easily seen from Fig. S2 where eLORETA-PSF-OA values are almost uniform, except for small areas under the grid having very high values (first row), while for MNE-PSF-OA values are larger than 0.5 under the ECoG electrodes and very low far from the grid (second row).

Contrarily, in eLORETA-CTF-OA deep sources under the ECoG electrodes and sources laying distant from the ECoG grid, such as those in the midline structures, are overestimated with respect to MNE. As seen in Fig. 3 and S1, the multimodal layout ECoG + EEG strongly decreases the resolution metrics far from the ECoG grid. The metric distributions over the cortex in eLORETA-CTF case (Fig. 5a) show that the scalp electrodes contralateral to the 128 channels ECoG grid lower DLE, SD and OA values of 50, 20 mm and a factor of 0.5, respectively. In MNE-CTF case (Fig. 5b) DLE and SD are lowered by 40 and 10 mm, while for the OA distribution there is an increase (up to a factor of 0.5) in the gyri profile, probably due to the bias of MNE in overestimating sources towards the electrodes. Finally, note that for eLORETA-CTF- and MNE-CTF-OA values in the midline structures do not change for the ECoG + EEG grid because this area is not covered by electrodes, neither ECoG or EEG, being the "Cz" electrode removed from the EEG grid for practical reasons (see also Fig. S3, third column).

High-Density EEG

To understand the importance of the number of EEG electrodes in the simultaneous layout, we investigated higher density electrode grid configuration using 73 electrodes with a 15 mm inter-electrode distance, which corresponds to the same spatial sampling of a 256 channels EEG grid in a human subject. Figure 6 shows the resolution metrics of this multimodal layout with high density EEG compared to the ones of the 128 channels ECoG grid, the 128 + 18 channels ECoG + EEG grid and the 73 channels EEG grid, all

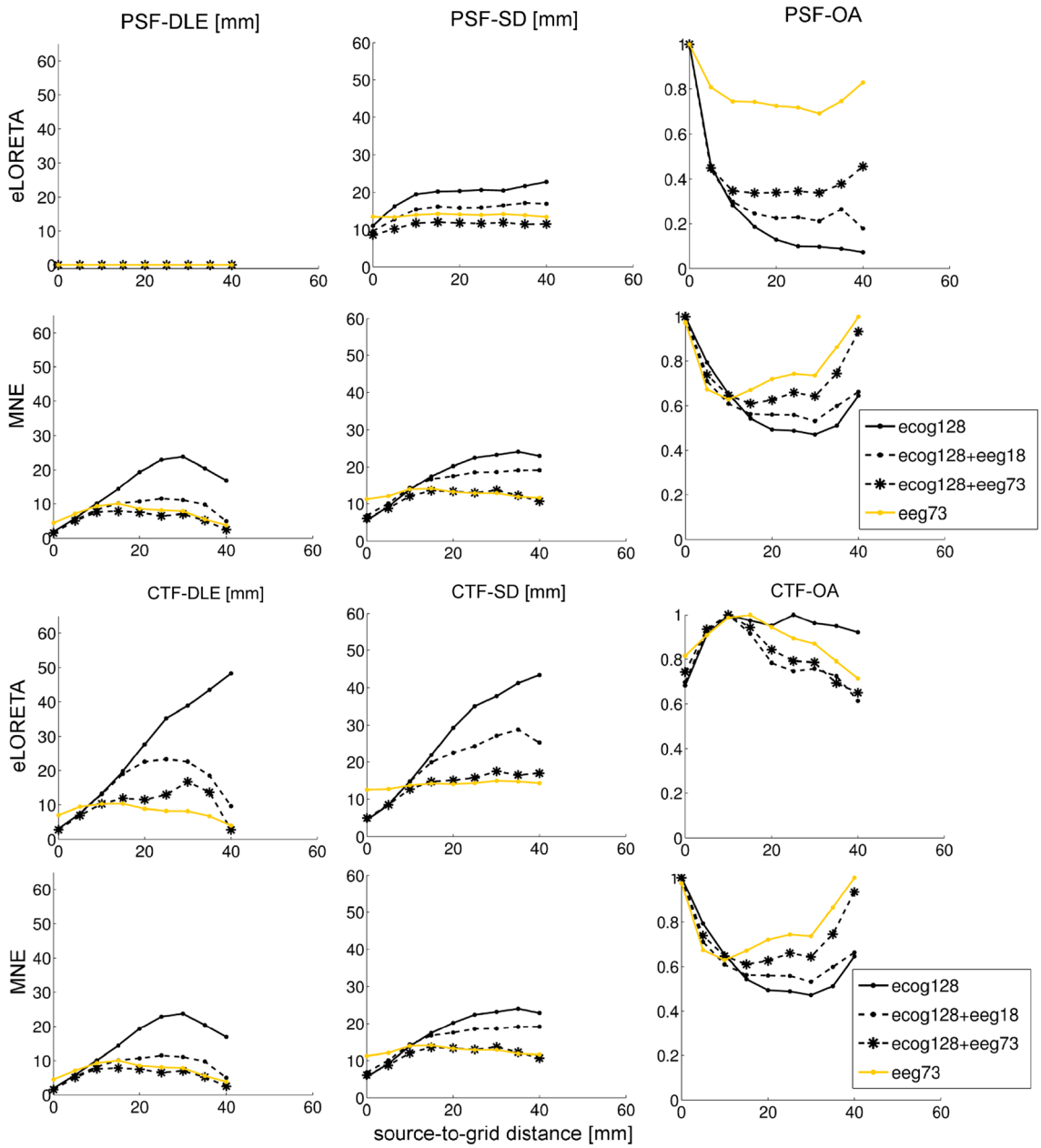

Fig. 6 Resolution metrics for the multimodal layout with 73 channels EEG grid as a function of the source-to-grid distance calculated for the distance classes of the 128 channels ECoG grid. The mean values of the PSF and CTF resolution metrics in each distance class, are calculated for the 128 channels ECoG grid (black solid line), 128 + 18 channels ECoG + EEG grid (black dotted line with circles), 128 + 73 channels ECoG + EEG grid (black dotted line with stars) and 73 channels EEG grid (yellow line) with eLORETA and MNE

calculated in the source-to-grid distance classes of the ECoG grid for a direct comparison.

As expected, increasing the number of EEG electrodes substantially improves the resolution for the sources distant from ECoG grid, the only exception being eLORETA-PSF-DLE which by construction is always equal to 0.

For eLORETA, the CTF-DLE and CTF-SD values of the ECoG + EEG grid with 128 + 73 channels decrease more rapidly than the multimodal layout with the 18 channels EEG as the source-to-grid distance increases, reaching the same value of the 73 channels EEG grid, i.e. around 5 and 15 mm in the last class, respectively. The eLORETA-PSF-SD metric of the 128 + 73 channels ECoG + EEG grid reaches the smaller values (around 10 mm) between all grid layouts, i.e. the 128 ECoG grid, the 128 + 18 channels ECoG + EEG grid and the 73 channels EEG grid, improving the performance of around 10, 5 and 2 mm, respectively. The PSF- and CTF-OA values

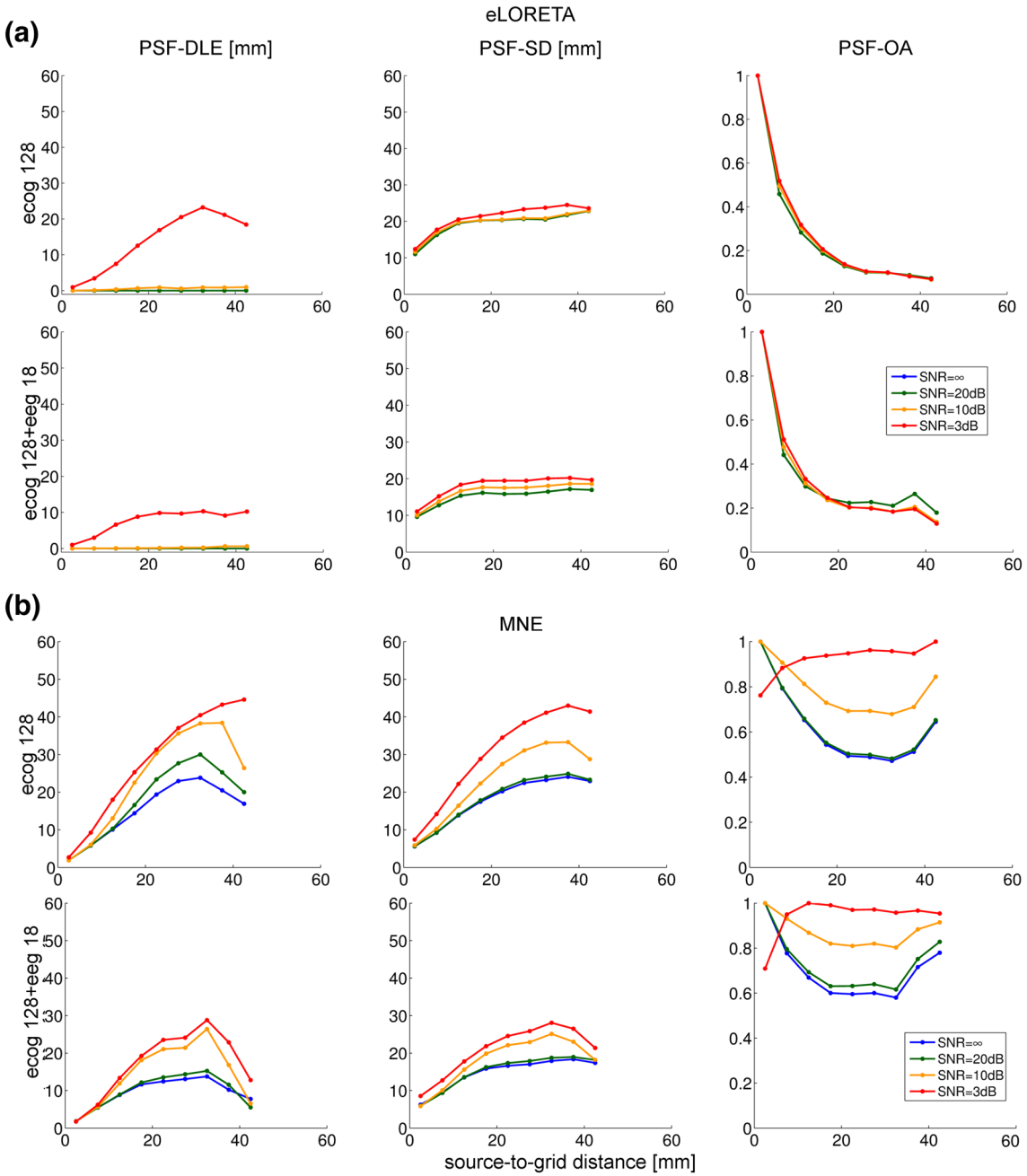

Fig. 7 Mean values of DLE, SD and OA for the 128 channels ECoG grid and the 128 + 18 channels ECoG + EEG grid obtained for the PSFs calculated with eLORETA (**a**) and MNE (**b**) from the noisy data, with SNR = 20, 10, and 3 dB (green, yellow and red lines) and in the noise-free data ("SNR= ∞", blue line)

of the ECoG + EEG grid with 128 + 73 channels increase with respect to the 128 + 18 channels ECoG + EEG grid, especially in the PSF case.

For MNE the comparison between the 128 + 73 and the 128 + 18 channels ECoG + EEG grids shows similar results. There is a slight decrease of DLE values of a few mm for the more distant sources. SD values decrease up to 10 mm as the source-to-grid distance increases, while the OA values highly increase (a factor of 0.3) far from the ECoG electrodes.

Influence of Gaussian Noise

Figure 7 shows the influence of Gaussian noise on eLORETA and MNE for different level of SNR, as a function of the source-to-grid distance classes. To investigate this

aspect, we calculate the resolution metrics described above on the "noisy PSF" of each source in the source space, i.e. we estimate the activity from the noisy measurements generated by a single dipolar source.

As expected, the errors on the resolution metrics increase when the SNR decreases, especially for DLE; furthermore, when the source-to-grid distance increases we observe an increment of the errors, i.e. the difference between values obtained in the noise-free case, referred to as "SNR $=\infty$" and other levels of SNR.

When the SNR is 20 dB, the values of DLE, SD and OA are comparable to the ideal values of the noise-free case, for each grid and both inverse methods.

When the SNR decreases below 20 dB, the performance of MNE worsens more than that of eLORETA, increasing the errors on the resolution metrics as the level of SNR decreases (Fig. 7b).

Note that, even for very low SNR (3 dB), DLE and SD values of the sources laying under the ECoG grid have very small difference with the values of the noise-free case for eLORETA and MNE, while this difference strongly increases for distant sources, especially for the DLE.

For low SNR, OA trend varies depending on the inverse algorithm. For eLORETA, the sources with higher OA values are always located under the ECoG electrodes, similarly to the noise-free case, while for MNE the OA profile can be completely reversed, probably due to the fact that in this study the MNE operator, described in Eq. (5), models the covariance matrix of the noise as the identity matrix.

Discussion

Being the ECoG grid placed directly on the cortical surface, this neuroimaging technique reaches high SNR and millimetric spatial resolution, but suffers from the limited field-of-view of the electrode grid. To infer brain activity at locations different from just below the electrode array, it is necessary to solve the electromagnetic inverse problem.

Results show that the source reconstruction obtained with eLORETA and MNE using ECoG data features good performance only for brain areas located directly under the grid, i.e. dipole localization error (DLE) and spatial dispersion (SD) under 10 mm for brain areas within 10 mm distance from the electrodes, while for distant sources the performance are poor. However, to fully exploit the results it is important to introduce some hypothesis on the cortical activity as well as to consider the experimental question. Some examples are given below.

If the experimental question is the spatial localization of an area which features a strong activity, much stronger than the rest of the cortex, then the PSF-DLE is the proper metric to be considered, since this metric quantifies the error in locating a source assuming that it is the only one active (indeed, PSF refers to Point-Spread Function). In this case, eLORETA is the correct choice, and the zero error for PSF-DLE assures that the source is correctly located even if it is far from the ECoG grid. However, if the dominant source is under the ECoG grid, MNE features a better compromise between localization accuracy and spatial dispersions than eLORETA, since eLORETA-PSF-SD values are much higher than those of MNE (the difference varies from 5 to 20 mm depending on the electrode number in the ECoG grid). This result is in line with previous studies (Zhang et al. 2008; Cho et al. 2011) which reported the reliability of MNE in the reconstruction of epileptogenic activity, modeled as extended sources, for high values of SNR (~20 dB).

If the experimental question is the spatial localization of the cortical activity during rest or when the activity is distributed over many cortical areas, then the CTF-DLE is the proper metric to be considered, since this metric quantifies the error in locating a source taking into account that the source activity may be due to the peak activity of a different cortical area (indeed CTF refers to Cross-Talk Function). In this case, eLORETA and MNE have similar performance, with slight better results under the grid for eLORETA, since DLE and SD rapidly increase as the distance between the sources and the electrodes increases.

Finally, if the experimental question is the characterization of the cortical activity during rest with the aim of investigating cortico-cortical connectivity, then the CTF-SD is the proper metric to be considered. Indeed, CTF-SD informs about how different brain areas (erroneously) contribute to the reconstructed activity of the voxel under study. Obviously, a high CTF-SD value will give rise to fake connectivity results, which are known as the "leakage effects" (Brookes et al. 2012; Hipp et al. 2012; Wens 2015; Van de Steen et al. 2016).

However, it is clear that reliable source reconstruction from ECoG data is possible just for neural activities laying in the proximity of the ECoG electrode grid. A possible solution to this problem is to simultaneously record ECoG with EEG data. This study shows that the combination of the ECoG with the EEG grid strongly increases the resolution properties of the reconstructed sources laying far from the ECoG grid with maximum DLE and SD values of about 25 mm. These results put emphasis on the impact that the limited field-of-view of the grid produces in source analysis. Indeed, we have shown that even few (18) scalp electrodes covering the whole cortical surface significantly improve the resolution of source estimates. Adding a higher density EEG grid (73 channels) further improves the resolution for sources distant from the ECoG grid. On the other hand, we note that there is a slight improvement underneath the ECoG grid when the multimodal setting is considered. A possible explanation is that the silastic sheet embedding the ECoG

electrodes negatively affects source reconstruction performance of scalp EEG only (Lanfer et al. 2013).

In our study, we integrated ECoG and EEG data by simply concatenating the two lead field matrices: more sophisticated techniques (Henson et al. 2009; Karahan et al. 2015) may optimize the fusion of the information gathered with each modality.

All the above considerations on the resolution matrix properties hold, by construction, for the noise-free case. A different approach must be taken to consider the influence of noise on those properties, as explained in the "Materials and Methods" section. Here, we superimpose Gaussian noise to the simulated potential of single dipoles located over the whole cortex in order to consider the effect of different levels of SNR on the resolution of the source reconstruction obtained from the ECoG grid and the ECoG + EEG grid. Our analysis shows that for high values of SNR (20 dB) the resolution metrics DLE, SD and OA are very similar to those obtained in the noise-free case, extending the validity of the previous results to more realistic situations. When the SNR decreases, the resolution metric values increase with the distance between the sources and the electrode, especially the DLE. Under the ECoG electrodes the influence of noise is remarkably low since the resolution properties for very low SNR (3 dB) are comparable to the ones of the noise-free case. The only exception is MNE-OA for low SNR, which has a reversed trend in respect to the noise-free case because the inverse operator is not take into account statistical properties of noise, e.g. the covariance (Dale et al. 2000).

Another possible strategy to take into account noise is to incorporate noise information directly into the inverse operator. In this case, considered by Molins et al. (2008), Hauk et al. (2011) and Hauk and Stenroos (2014) the resolution matrix is again defined as the product between the inverse operator and the lead field matrix, with the same interpretation for the Point-Spread Function and the Cross-Talk Function. The difference between the two approaches is that, in our case, the resolution matrix relates the actual configuration of sources with the estimated one, while in the other case this relationship, which is made under the noise-free assumption, is not well-defined. Nevertheless, it seems reasonable to think that the better is the "suppression" of noise achieved with the inverse operator, the more reliable is the resolution matrix (in the sense that it truly relates the actual configuration of sources with the estimated ones). Our simulations in the presence of noise give credits to this last statement, as indeed for decreasing level of SNR the results obtained with eLORETA, are more robust than those of MNE.

The current analysis describes the resolution of source localization methods in the cortex of a rhesus macaque from ECoG and EEG measurements. In the literature, studies on monkeys have been a key element in understanding structural and functional mechanisms of brain structures, from cellular to whole-brain level (Zeki 1978; Wandell et al. 2007). On the anatomical level, the major difference is that the monkey cortex is about half of the human cortex, i.e. $6 \times 6 \times 4$ cm and $15 \times 11 \times 11$ cm, respectively, (see Fig. S4).

A detailed comparison between human and monkey brains is beyond the aim of this article, but being the shape of the monkey cortex sufficiently similar to the human one, it can be reasonably used as a model to evaluate the resolution of inverse methods as a function of the distance between small patches of cortical areas and ECoG or EEG electrodes. Reasonably, the resolution metrics will have the similar values near the grid in the monkey and in the human case, while far from the grid, as the source-to-grid distance reaches higher values, errors as quantified by the given resolution metrics could further increase.

Given the growing interest of the activity of subcortical areas in cognitive mechanisms and brain disorders (Bastin et al. 2017; Combrisson et al. 2017; Kim et al. 2010; Morino et al. 2004), another useful application of ECoG source analysis could be to estimate subcortical activity, e.g. from the hippocampus, the amygdala, the thalamus, the cerebellum, the insula. In principle, ECoG grid could be a useful tool for studying deep brain regions because it has a wider coverage than stereo-tactically implanted electrodes (sEEG) and it has a higher SNR than MEG and EEG. Even if we cannot draw conclusion on this issue, since the subcortical areas are not included in the dataset used in this manuscript, our analysis suggests that unless the ECoG grid is positioned up to 5–10 mm near the region of interest, the source analysis could lead to unreliable results. Nevertheless, by using more restrictive assumption about the source configuration one can, in principle, improve the accuracy of source localization techniques for deep sources. For example, new inverse methods can be designed through the resolution matrix imposing the subcortical areas as active region of interest while filtering out the activity originating from the cortex, e.g. by imposing a topological constraint for the Cross-Talk Functions (Hauk and Stenroos 2014).

Conclusions

In conclusion, this study quantifies the limits of source reconstruction from ECoG grid with different resolution metrics, such as dipole localization error, spatial dispersion and overall amplitude, and could be used to choose the "optimal" inverse algorithm based on its resolution properties.

As a possible remedy to the poor performance obtained far from the ECoG grid, we evaluated the improvements in source reconstruction when simultaneous recordings of ECoG and EEG potentials are available, even with a limited number of EEG electrodes. Further studies aiming to

improve ECoG source analysis could involve the design of new inverse algorithms which specifically take into account the limited coverage of the ECoG grid and also the complementary features of ECoG and EEG.

Acknowledgements We would like to thank Pedro A. Valdés Sosa, Daniele Marinazzo and Dezhong Yao for the organization and realization of the workshop and the special issue on the "Controversies in EEG Source Analysis". We also thank Shiang Hu for the kind suggestions regarding the high density EEG grid lead field calculation

References

Bastin J, Deman P, David O, Gueguen M, Benis D, Minotti L, Hoffman D, Combrisson E, Kujala J, Perrone-Bertolotti M, Kahane P, Lachaux JP, Jerbi K (2017) Direct recordings from human anterior insula reveal its leading role within the error-monitoring network. Cereb Cortex 27:1545–1557

Brookes MJ, Woolrich MW, Barnes GR (2012) Measuring functional connectivity in MEG: a multivariate approach insensitive to linear source leakage. NeuroImage 63:910–920

Chella F, Pizzella V, Zappasodi F, Marzetti L (2016) Impact of the reference choice on scalp EEG connectivity estimation. J Neural Eng 13(3):036016. https://doi.org/10.1088/1741-2560/13/3/036016

Cho JH, Hong SB, Jung YJ, Kang HC, Kim HD, Suh M, Jung KY, Im CH (2011) Evaluation of algorithms for intracranial EEG (iEEG) source imaging of extended sources: feasibility of using iEEG source imaging for localizing epileptogenic zones in secondary generalized epilepsy. Brain Topogr 24:91–104

Combrisson E, Perrone-Bertolotti M, Soto JLP, Alamian G, Kahane P, Lachaux JP, Guillot A, Jerbi K (2017) From intentions to actions: Neural oscillations encode motor processes through phase, amplitude and phase-amplitude coupling. Neuroimage 147:473–487

Crone N, Miglioretti D, Gordon B, Lesser R (1998) Functional mapping of human sensorimotor cortex with electrocorticographic spectral analysis. II. Event-related synchronization in the gamma band. Brain 121:2301–2315

Daitch AL, Sharma M, Roland JL, Astafiev SV, Bundy DT, Gaona CM, Snyder AZ, Shulman GL, Leuthardt EC, Corbetta M (2013) Frequency-specific mechanism links human brain networks for spatial attention. Proc Natl Acad Sci USA 110:19585–19590

Dale AM, Liu AK, Fischl BR, Buckner RL, Belliveau JW, Lewine JD, Halgren E (2000) Dynamic statistical parametric mapping: combining fMRI and MEG for high-resolution imaging of cortical activity. Neuron 26(1):55–67

de Gooijer-van de Groep KL, Leijten FSS, Ferrier CH, Huiskamp GJM (2013) Inverse modeling in magnetic source imaging: comparison of MUSIC, SAM(g2), and sLORETA to interictal intracranial EEG. Hum Brain Mapp 34:2032–2044

Ding L, Wilke C, Xu B, Xu X, van Drongelen W, Kohrman M, He B (2007) EEG source imaging: correlating source locations and extents with electrocorticography and surgical resections in epilepsy patients. J Clin Neurophysiol 24(2):130–136

Dümpelmann M, Fell J, Wellmer J, Urbach H, Elger CE (2009) 3D source localization derived from subdural strip and grid electrodes: a simulation study. Clin Neurophysiol 120:1061–1069

Dümpelmann M, Ball T, Schulze-Bonhage A (2012) sLORETA allows reliable distributed source reconstruction based on subdural strip and grid recordings. Hum Brain Mapp 33:1172–1188

Grech R, Cassar T, Muscat J, Camilleri KP, Fabri SG, Zervakis M, Xanthopoulos P, Sakkalis V, Vanrumste B (2008) Review on solving the inverse problem in EEG source analysis. J Neuro-eng Rehabil 5:25

Gunduz A, Brunner P, Daitch A, Leuthardt EC, Ritaccio AL, Pesaran B, Schalk G (2012) Decoding covert spatial attention using electrocorticographic (ECoG) signals in humans. Neuroimage 60:2285–2293

Hämäläinen MS, Hari R, Ilmoniemi RJ, Knuutila J, Lounasmaa OV (1993) Magnetoencephalography-theory, instrumentation, and applications to noninvasive studies of the working human brain. Rev Mod Phys 65:413–497

Hauk O, Stenroos M (2014) A framework for the design of flexible cross-talk functions for spatial filtering of EEG/MEG data: DeFleCT. Hum Brain Mapp 35:1642–1653

Hauk O, Wakemanm DG, Henson R (2011) Comparison of noise-normalized minimum norm estimates for MEG analysis using multiple resolution metrics.Neuroimage 54:1966–1974

Henson RN, Mouchlianitis E, Friston KJ (2009) MEG and EEG data fusion: simultaneous localisation of face-evoked responses. NeuroImage 47(2):581–589

Hipp JF, Hawellek DJ, Corbetta M, Siegel M, Engel AK (2012) Large-scale cortical correlation structure of spontaneous oscillatory activity. Nat Neurosci 15:884–890

Karahan E, Rojas-López PA, Bringas-Vega ML, Valdés-Hernández PA, Valdes-Sosa PA (2015) Tensor analysis and fusion of multimodal brain images. Proc IEEE 103(9):1531–1559

Kim JS, Im CH, Jung YJ, Kim EY, Lee SK, Chung CK (2010) Localization and propagation analysis of ictal source rhythm by electrocorticography. NeuroImage 52:1279–1288

Koles ZJ (1998) Trends in EEG source localization. Electroencephalogr Clin Neurophysiol 106(2): 127–137

Lanfer B, Röer C, Scherg M, Rampp S, Kellinghaus C, Wolters C (2013) Influence of a silastic ECoG grid on EEG/ECoG based source analysis. Brain Topogr 26:212–228

Lin FH, Witzel T, Ahlfors SP, Stufflebeam SM, Belliveau JW, Hämäläinen MS (2006) Assessing and improving the spatial accuracy in MEG source localization by depth-weighted minimum-norm estimates. Neuroimage 31:160–171

Liu Y, Coon WG, de Pesters A, Brunner P, Schalk G (2015) The effects of spatial filtering and artifacts on electrocorticographic signals. J Neural Eng 12:056,008

Marzetti L, Nolte G, Perrucci GM, Romani GL, Del Gratta C (2007) The use of standardized infinity reference in EEG coherency studies. Neuroimage 36:48–63

Mesgarani N, Chang EF (2012) Selective cortical representation of attended speaker in multi-talker speech perception. Nature 485(7397), https://doi.org/10.1038/nature11020

Michel CM, Murray MM, Lantz G, Gonzalez S, Spinelli L, Grave de Peralta R (2004) EEG source imaging. Clin Neurophysiol 115(10):2195–2222

Molins A, Stufflebeam SM, Brown EN, Hämäläinen MS (2008) Quantification of the benefit from integrating MEG and EEG data in minimum l2 -norm estimation. Neuroimage 42(3):1069–1077

Morino M, Ishibashi K, Hara M (2004) Surgical treatment of temporal lobe epilepsy associated with subcortical ectopic gray matter under the guidance of intraoperative electrocorticography. Seizure 13:470–474

Nagasaka Y, Shimoda K, Fujii N (2011) Multidimensional recording (MDR) and data sharing: an ecological open research and educational platform for neuroscience. PLoS ONE 6:e22561 https://doi.org/10.1371/journal.pone.0022561

Neuper C, Klimesch W (2006) Event-related dynamics of brain oscillations. Elsevier, Amsterdam

Oostenveld R, Fries P, Maris E, Schoffelen JM (2011) Fieldtrip: open source software for advanced analysis of MEG, EEG, and invasive electrophysiological data. Comput Intell Neurosci. https://doi.org/10.1155/2011/156869

Ortega GJ, Sola RG, Pastor J (2008) Complex network analysis of human ECoG data. Neurosci Lett 447:129–133

Papadopoulou M, Friston K, Marinazzo D (2015) Estimating directed connectivity from cortical recordings and reconstructed sources. Brain Topogr. https://doi.org/10.1007/s10548-015-0450-6

Pascarella A, Todaro C, Clerc M, Serre T, Piana M (2016) Source modelling of ElectroCorticoGraphy (ECoG) data: stability analysis and spatial filtering. J Neurosci Methods. https://doi.org/10.1016/j.jneumeth.2016.02.01

Pascual-Marqui RD (2007) Discrete, 3D distributed, linear imaging methods of electric neuronal activity. Part 1: exact, zero error localization. http://arxiv.org/pdf/0710.3341

Potes C, Gunduz A, Brunner P, Schalk G (2012) Dynamics of electrocorticographic (ECoG) activity in human temporal and frontal cortical areas during music listening. Neuroimage 61:841–848

Sugano H, Shimizu H, Sunaga S (2007) Efficacy of intraoperative electrocorticography for assessing seizure outcomes in intractable epilepsy patients with temporal-lobe-mass lesions. Seizure 16:120–127

Takaura K, Tsuchiya N, Fujii N (2016) Frequency-dependent spatiotemporal profiles of visual responses recorded with subdural ECoG electrodes in awake monkeys: differences between high- and low-frequency activity. Neuroimage 124:557–572

Van de Steen F, Faes L, Karahan E, Songsiri J, Valdes-Sosa PA, Marinazzo D (2016) Critical comments on EEG sensor space dynamical connectivity analysis. Brain Topogr. https://doi.org/10.1007/s10548-016-0538-7

Wandell BA, Dumoulin SO, Brewe AA (2007) Visual field maps in human cortex. Neuron. https://doi.org/10.1016/j.neuron.2007.10.012

Watrous AJ, Deuker L, Fell J, Axmacher N (2015) Phase-amplitude coupling supports phase coding in human ECoG. eLife 4(886):e07. https://doi.org/10.7554/eLife.07886

Wens V (2015) Investigating complex networks with inverse models: analytical aspects of spatial leakage and connectivity estimation. Phys Rev E 91:012823

Yanagawa T, Chao ZC, Hasegawa N, Fujii N (2013) Large-scale information flow in conscious and unconscious states: an ECoG study in monkeys. PLoS ONE 8:1–13

Zeki SM (1978) Uniformity and diversity of structure and function in rhesus monkey prestriate visual cortex. J Physiol 277:273–290

Zhang Y, van Drongelen W, Kohrman M, He B (2008) Three-dimensional brain current source reconstruction from intra-cranial ECoG recordings. Neuroimage 42:683–695

Affiliations

Chiara Todaro[1] · Laura Marzetti[1,2] · Pedro A. Valdés Sosa[3,4] · Pedro A. Valdés-Hernandez[5] · Vittorio Pizzella[1,2]

1 Department of Neuroscience, Imaging and Clinical Sciences, University "G d'Annunzio" of Chieti-Pescara, Via Luigi Polacchi 11, 66013 Chieti, Italy

2 Institute for Advanced Biomedical Technologies, University "G d'Annunzio" of Chieti-Pescara, Via Luigi Polacchi 11, 66013 Chieti, Italy

3 The Clinical Hospital of Chengdu Brain Science Institute, MOE Key Lab for Neuroinformation, University of Electronic Science and Technology of China, Chengdu, China

4 Cuban Neuroscience Center, Havana, Cuba

5 Florida International University, Miami, FL, USA